www.springer.com/41230
https://doi.org/10.1007/s41230-026-5102-9

Effect of SiO_2 content and sintering temperature on Al_2O_3 ceramic cores by stereolithography

***Ren-xiao Zou[1, 2], Shao-kui Yin[1, 2], Zhi-yong Yu[1], Rui-long Yu[1, 2], Ying-wei Zhou[1, 2], Yue-ting Ma[1, 2], and Peng-wei Wang[1, 2]**

1. Shenyang Research Institute of Foundry Co., Ltd. CAM, Shenyang 110022, China

2. State Key Laboratory of Advanced Casting Technologies, Shenyang 110022, China

Copyright © 2026 Foundry Journal Agency

Abstract: Ceramic core is crucial to the production of precise and complex hollow blades. However, traditional manufacturing methods have struggled to achieve the stringent requirements. In contrast, a highly efficient method for manufacturing ceramic cores has been offered by 3D printing technology. In this study, Al_2O_3 ceramic cores were fabricated by stereolithography (SLA), a type of 3D printing technology, and the effects of SiO_2 content and sintering temperature on their performance were investigated. Results show that during the sintering process, SiO_2 reacts with Al_2O_3 in the solid phase to form mullite. As the degree of densification increases, sintered necks develop between larger and smaller particles. Mullite possesses high strength and excellent high-temperature creep resistance, thereby enhancing the strength and high-temperature creep resistance of the ceramic cores. When the silica content is 20% and the sintering temperature is 1,400 °C, the ceramic core exhibits the optimal performance with an open porosity of 20.4% and a bulk density of 1.42 g·cm^{-3}. It presents low dimensional shrinkage, with values of 2.59%, 3.59%, and 2.75% along the *x*-, *y*-, and *z*-directions, respectively. It possesses a flexural strength of 21.08 MPa at room temperature and 24.70 MPa at 1,350 °C, along with a high temperature deflection of 0.7 mm. These properties satisfy the casting criteria for complex hollow blades, indicating excellent high-temperature performance.

Keywords: SLA; ceramic core; SiO_2; sintering temperature; high-temperature performance; hollow blades

CLC numbers: TG221$^+$.1 **Document code:** A **Article ID:** 1672-6421(2026)06-919-10

1 Introduction

Recent advances in aviation technology worldwide have focused on improving the temperature resistance of turbine blades, aiming to raise the thrust-to-weight ratio of aero-engines, the critical components widely known as the "heart of aviation"[1-3]. Contemporary turbine blades demonstrate exceptional thermal stability, with temperature resistance exceeding 2,000 K[4, 5]. Three primary approaches have been developed to further improve the high-temperature capability of blades: (1) development of advanced alloy materials, though limited by fundamental metallic melting points; (2) application of thermal barrier coatings to enhance surface thermal resistance[6]; and (3) implementation of ceramic cores to create sophisticated internal cooling channels that improve heat dissipation through air cooling[7-9], thereby increasing overall temperature-bearing capacity. These developments underscore the crucial role of ceramic cores in determining final blade quality[10].

Ceramic core typically consists of refractory matrix materials, mineralizers, plasticizers, and supplementary additives. Current classification systems divide ceramic cores into silicon-based and aluminum-based varieties according to their matrix materials[9, 11]. Among them, α-Al_2O_3 emerges as the preferred matrix material due to its exceptional properties: an operational temperature ceiling of 1,875 °C, outstanding chemical stability, absence of phase transformations, and minimal reactivity with active elements[12]. Furthermore, its thermal expansion characteristics exhibit excellent compatibility with shell materials at elevated temperatures[13]. The remarkable stability of α-Al_2O_3 originates from its crystalline structure, where Al^{3+} ions occupy octahedral interstices formed by O^{2-} ions[14].

***Ren-xiao Zou**

Male, Master. His research interests primarily focus on 3D printing technologies, especially alumina ceramics.

E-mail: 15542412983@163.com

Received: 2025-05-06; Revised: 2025-12-01; Accepted: 2026-06-18

Modern applications of ceramic cores require stringent performance specifications and tight dimensional tolerances. Conventional fabrication techniques, including hot press molding, gel injection molding, and traditional injection molding, struggle to balance high production efficiency and cost-effectiveness[15]. This technological gap has created an urgent need for alternative manufacturing approaches capable of producing complex, precision ceramic cores[7]. In this context, SLA offers several distinct advantages: (1) simplified manufacturing of geometrically complex components; (2) excellent substrate stability and processability; (3) reduced costs and improved efficiency for rapid design verification; and (4) environmentally sustainable operation with material recyclability[16]. These characteristics make SLA particularly suitable for rapid prototyping of precision ceramic cores.

Existing research on 3D-printed Al_2O_3 ceramics has primarily focused on several areas: ceramic mold fabrication[17, 18], particle size optimization[19-21], debinding process development[21-23], and investigations of plasticizer effects[24]. In parallel, studies have explored the application of photocuring technology for the production of aero-engine blade cores[25-28]. Li et al.[29] found that when the mass ratio of coarse, medium, and fine alumina particles was 2:1:1 and the sintering temperature was 1,600 °C, the alumina ceramic core prepared via SLA exhibited an open porosity of 36.4%, a high-temperature deflection of 2.27 mm, and a flexural strength of 50.1 MPa. Meng[6] also prepared alumina ceramic cores via SLA. The cores sintered at 1,500 °C exhibited a flexural strength of 16.6 MPa and an open porosity of 37.03%. Excessively high sintering temperatures impose stringent demands on production equipment, thereby limiting their potential for industrial applications. Multiple studies have examined the influence of silica sol and other SiO_2-containing additives on core performance[6, 30-35]. These studies demonstrate that although SiO_2 incorporation improves Al_2O_3 ceramic core performance compared to alternative mineralizers, significant limitations persist. Notably, maximum flexural strength of nano-silica modified cores reaches only 13.8 MPa, falling short of practical application requirements[34]. Even with the addition of silicone resin and sintering at 1,500 °C, the flexural strength fails to reach 20 MPa at 1,350 °C, indicating inadequate high-temperature performance[30]. These findings highlight the necessity for systematically optimizing the interplay among the SiO_2 content, sintering temperature, and final performance relationship to enable practical application of 3D-printed alumina ceramic cores.

This study addresses these challenges through controlled variation of SiO_2 content and sintering temperature in ceramic core fabrication. The resulting phase constitution, sintering behavior, and mechanical properties were comprehensively characterized to achieve the following research objectives:

(1) optimize the SiO_2 content;

(2) determine the ideal sintering temperatures; and

(3) reduce the sintering temperature while minimizing shrinkage and enhancing high-temperature performance of Al_2O_3 ceramic cores.

2 Experimental procedure

2.1 Materials and sample preparation

Sample preparation includes preparation and printing of materials, and degreasing and sintering of green bodies. The slurry consisted of ceramic powder, mineralising agent, and photosensitive resin. The ceramic powders are spherical Al_2O_3 with a particle size of 1–5 μm (99.99wt.% purity, Anhui Zhonghang Nano Science and Technology Development Co., Ltd.), and the mineralising agent was composed of SiO_2 with a particle size of 1 μm (99.99wt.% purity, Anhui Zhonghang Nano Science and Technology Development Co., Ltd.). The photosensitive resin comprised HDDA, NPG2PODA, TMPTA, and TXIB (Shanghai Youying Chemical Technology Co., Ltd.), with a mass ratio of 43:17:10:30. The 500 g of Al_2O_3 and SiO_2 (5%, 10%, 15%, 20%, and 25% in weight) was weighed and dried at 200 °C for 12 h. The 10 g of BYK-9076 dispersant was added to the anhydrous ethanol, mixed and added to the dry powder. After ball milling for 0.5 h, the mixture was dried naturally for 12 h to obtain the modified powder. Then, the modified powder was added to the photosensitive resin and homogenized with a homogenizer (Shenzhen Zhongyi Technology Co., Ltd.) to obtain the ceramic slurry with the viscosity of 6.50 Pa·s. An SLA printer (Kangshuo Intelligent Manufacturing Co., Ltd., as schematically illustrated in Fig. 1) was used. The printing process employed a top-down configuration with an exposure power of 40 mw·cm^{-2}, a scanning speed of 5,000 mm·s^{-1}, and a layer thickness of 50 μm.

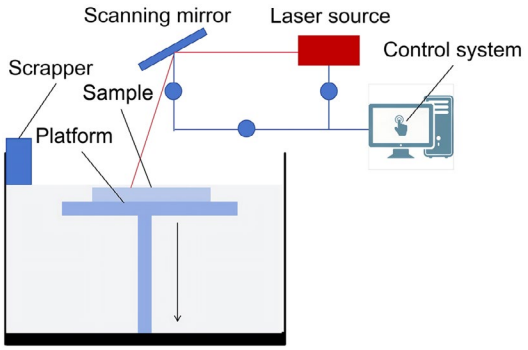


Fig. 1: Schematic diagram of SLA device

The degreasing and sintering steps were as follows: First, the samples were placed in a resistance furnace. After nitrogen filling, they were slowly heated to 240 °C at a heating rate of 0.2 °C·min^{-1} and held for 20 min. At the same heating rate, the temperature was further increased to 460 °C and held for another 20 min. Subsequently, the heating rate was set to 0.3 °C·min^{-1}, and the temperature was slowly raised to 800 °C and held for 120 min. Finally, the temperature was increased to 1,050 °C at a heating rate of 0.5 °C·min^{-1} and held for 5 min, followed by heating to the sintering temperature T (T=1,250; 1,300; 1,350; 1,400; and 1,450 °C) at 3 °C·min^{-1}. The samples were held at this temperature for 90 min and then furnace cooled to room temperature. After degreasing and sintering, the Al_2O_3 ceramic core samples were obtained.

2.2 Measurements of open porosity and density

Archimedes' method[36] was used for the measurements of open porosity and density. Three samples from each group were dried and weighed three times to obtain the average dry weight (M_1). The samples were then immersed in deionised water under vacuum until no air bubbles were observed. Subsequently, the samples were removed and their suspended weight was measured three times to obtain the average value (M_3). The surface water of the samples was wiped off using filter paper and the wet weight (M_2) was measured three times to obtain the average value. The open porosity (B) and bulk density (ρ) of the samples were calculated using the following equations:

$$B = \frac{M_2-M_1}{M_2-M_3} \times 100\% \quad (1)$$

$$\rho = \frac{M_1 \times \rho_{water}}{M_2-M_3} \quad (2)$$

where ρ_{water} is the density of deionized water at the test temperature.

2.3 Shrinkage rate

Dimensions of the SLA and sintered samples were measured three times in different directions and positions using a vernier caliper with an accuracy of 0.02 mm, and the average value was recorded. The sintering shrinkage (δ) was calculated using the following equation:

$$\delta = \frac{L-L_1}{L} \times 100\% \quad (3)$$

where L is the sample length before sintering and L_1 is the length after sintering.

2.4 Mechanical testing

The flexural strength of the samples was measured at both room temperature and 1,300 °C using specimens with dimensions of 60 mm×10 mm×4 mm. The flexural strength (σ_W) was calculated according to Eq. (4):

$$\sigma_W = \frac{3PL_0}{2bH^2} \quad (4)$$

where P is the load when the sample was broken, L_0 is the span between two fulcrums, b is the width, and H is the thickness.

2.5 Deflection

The sample for measuring the high-temperature deflection was measured 120 mm×10 mm×4 mm. The height from the endpoint of the sample which is away from the specimen holder to the bottom of the specimen holder before heating is designated as H_1, while the corresponding distance after cooling is designated as H_2. Then, the high-temperature deflection $\Delta H = H_1 - H_2$.

2.6 Microstructural characterization

Scanning electron microscopy [SEM, Hitachi Scientific Instruments (Beijing) Co., Ltd., SU3500, China] with an accelerating voltage of 15 kV was used to evaluate the fracture surface of the Al_2O_3 ceramic core, and an X-ray energy spectrum analyzer (EDS) was employed to observe the elemental distributions. The phases of the ceramic cores at different silica contents and sintering temperatures were determined using an X-ray diffractometer (XRD: Bruker, D8 advance, Germany).

3 Results and discussion

3.1 Microstructure and phase constitution

Figure 2 shows the XRD images of Al_2O_3 ceramic cores with different SiO_2 contents (sintered at 1,300 °C) and sintering temperatures (with 20% SiO_2). As shown in Fig. 2(a), when SiO_2 is 5%, the peak intensity of SiO_2 is low. At this time, there is little mullite phase, only SiO_2 and Al_2O_3 can be detected. When the SiO_2 content continues to increase, the intensity of the SiO_2 peak increases significantly. However, as the SiO_2 content exceeds 20%, the peak intensity of SiO_2 begins to decrease, due to the reaction between SiO_2 and Al_2O_3 to form mullite. Nevertheless, at a sintering temperature of 1,300 °C, the solid-state reaction yields a limited amount of the mullite phase, resulting in an indistinct diffraction peak. As shown in Fig. 2(b), when the sintering temperatures are 1,250 °C and 1,300 °C, the SiO_2 peaks are distinct, whereas the mullite peaks are indistinct. When the sintering temperature is higher than 1,350 °C, the mullite peaks become obvious, and their

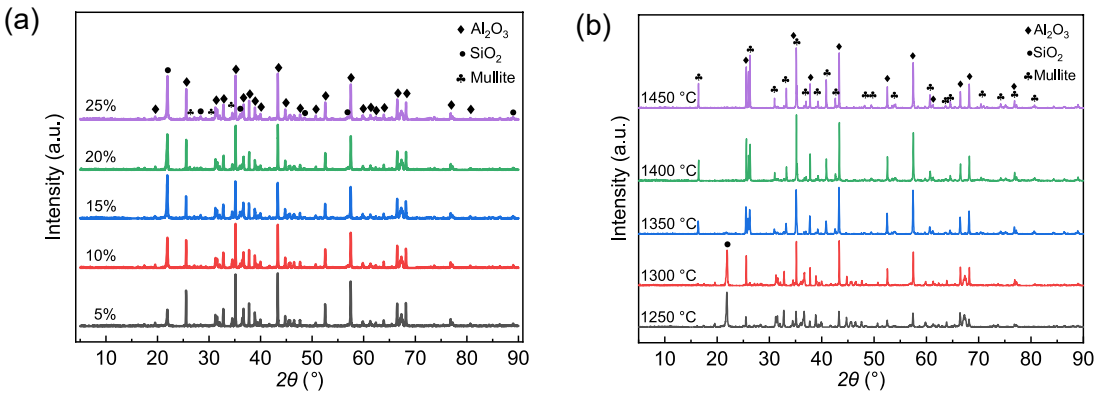


Fig. 2: Phase constitution of Al_2O_3 ceramic cores after sintering: (a) with different SiO_2 contents sintered at 1,300 °C; (b) with 20% SiO_2 sintered at different temperatures

intensity increases with the increase of sintering temperature due to the promoted reaction between SiO_2 and Al_2O_3.

The fracture morphology analysis of Al_2O_3 ceramic cores with varying SiO_2 contents (5%, 10%, 15%, 20%, and 25%) sintered at 1,300 °C (Fig. 3) reveals distinct microstructural evolution. Interparticle porosity is clearly observable, with pore density exhibiting an inverse relationship to SiO_2 content. During the thermal debinding and sintering processes, organic resin components undergo complete pyrolysis at 1,050 °C, leaving behind residual voids that subsequently evolve into structural pores. Concurrently, the formation of sintering necks between particles generates additional porosity within the ceramic matrix[33, 37].

Microstructural examination demonstrates in Figs. 3(a) and (b), where larger Al_2O_3 particles form a continuous skeletal network, while finer particles occupy interparticle voids. At lower SiO_2 concentrations (5%–10%), fewer sintering necks form. However, with increasing SiO_2 content (15%–25%), enhanced liquid phase sintering promotes significant sintering neck growth, as evidenced in Figs. 3(c)–(e).

Figure 4 shows the fracture morphology of Al_2O_3 ceramic cores with 20% SiO_2 at different sintering temperatures. It can be seen that when the sintering temperature increases from 1,250 °C to 1,450 °C, the number of pores in the ceramic core decreases significantly. However, the number of sintering necks increases significantly, mainly forming between smaller particles, while the larger particles act as the structural skeleton, and are tightly surrounded by the smaller ones.

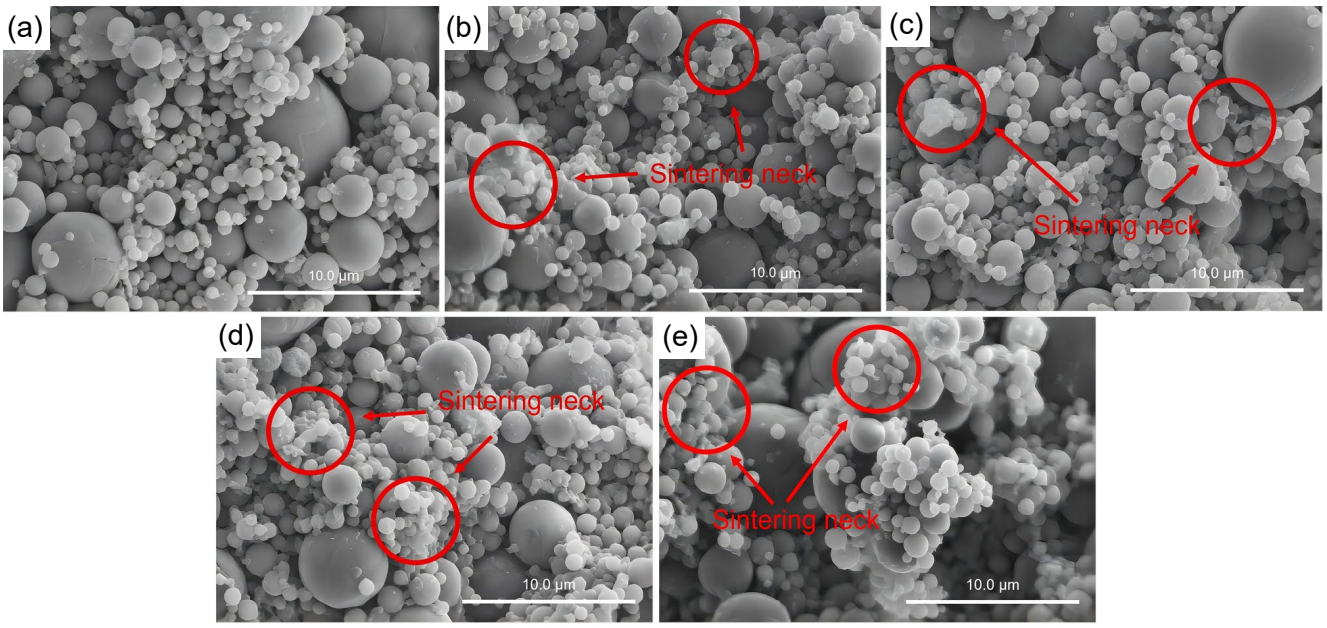


Fig. 3: Fracture morphologies of Al_2O_3 ceramic cores with different SiO_2 contents sintered at 1,300 °C: (a) 5%; (b) 10%; (c) 15%; (d) 20%; (e) 25%

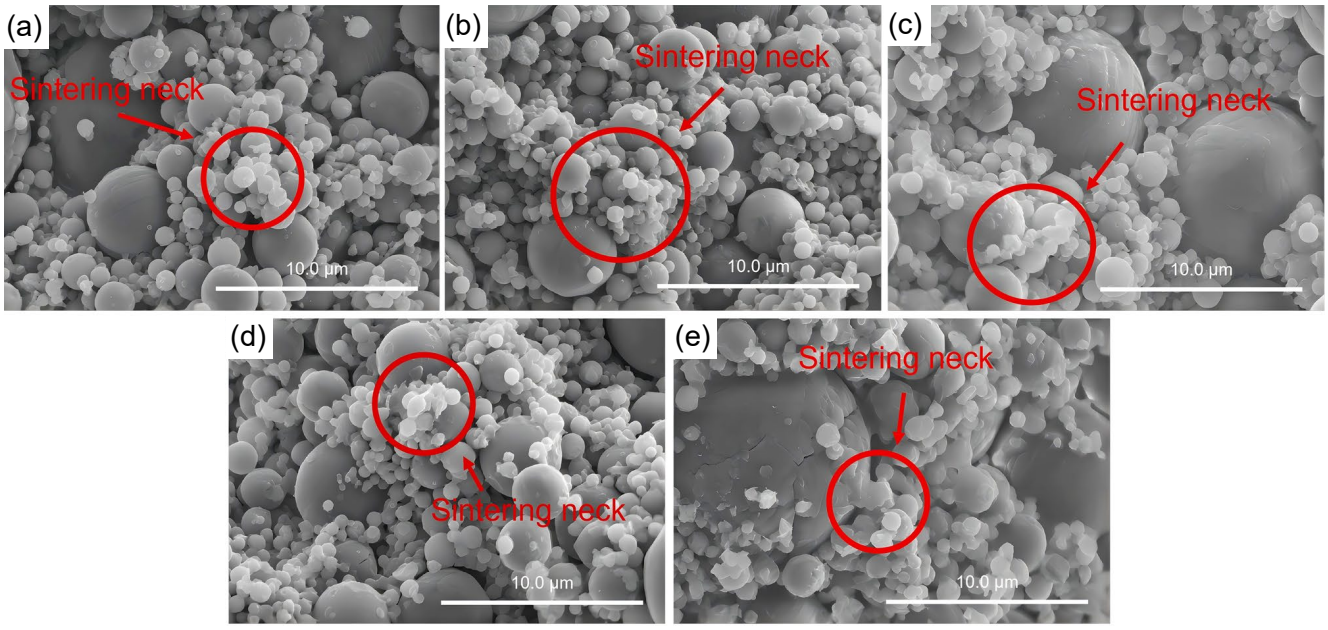


Fig. 4: Fracture morphologies of Al_2O_3 ceramic cores with 20% SiO_2 sintered at different temperatures: (a) 1,250 °C; (b) 1,300 °C; (c) 1,350 °C; (d) 1,400 °C; (e) 1,450 °C

Figure 5 shows the morphology and element distribution of the ceramic core with a SiO_2 content of 25% sintered at 1,300 °C. From the EDS results, it can be seen that the large particles are Al_2O_3. The spatial overlap of the Al, Si, and O elemental distributions in Figs. 5(b)–(d) suggests the formation of a single phase. Given that mullite is the sole thermodynamic product of SiO_2 and Al_2O_3, these EDS observations, in conjunction with the XRD results in Fig. 2, confirm the generation of mullite phase.

Figure 6 shows the morphology and element distribution of the ceramic core contained 20% SiO_2 sintered at 1,450 °C. As shown in Fig. 6(a), the large particles are tightly surrounded by small particles, and there are a large number of sintering necks between the large and small particles. EDS mapping reveals that, compared to the core sintered at 1,300 °C with 25% SiO_2, the Al, Si and O elemental distributions in Figs. 6(b), (c) and (d) exhibit a significantly enhanced spatial overlap. This pronounced coincidence, further corroborated by the XRD patterns in Fig. 2, indicates a substantial increase in the mullite phase.

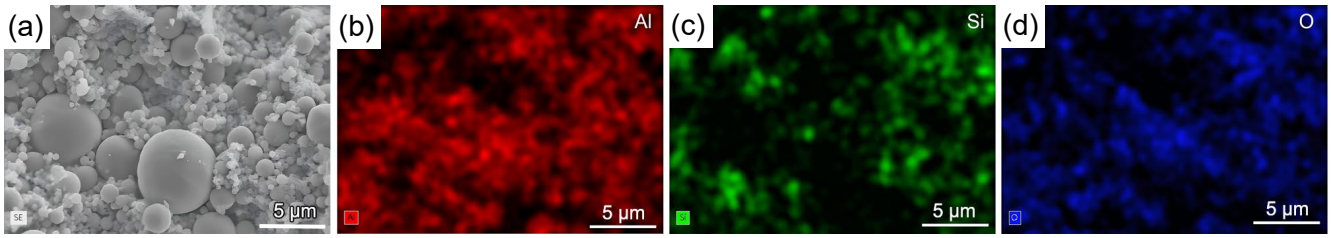


Fig. 5: SEM image (a) and element distribution of Al_2O_3 ceramic cores with 25% SiO_2 sintered at 1,300 °C: (b) Al; (c) Si; (d) O

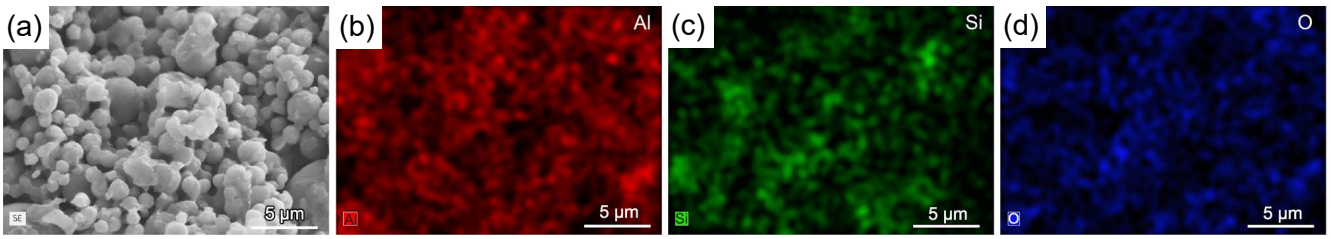


Fig. 6: SEM image (a) and element distribution of Al_2O_3 ceramic cores with 20% SiO_2 sintered at 1,450 °C: (b) Al; (c) Si; (d) O

3.2 Influence of SiO_2 content and sintering temperature on shrinkage

Figures 7(a) and (b) show the shrinkage curves of Al_2O_3 ceramic cores as a function of SiO_2 content (sintered at 1,300 °C) and sintering temperature (with 20% SiO_2). It can be seen that both SiO_2 content and sintering temperature have an effect on the shrinkage of Al_2O_3 ceramics, and the effect of SiO_2 content is greater than that of sintering temperature. Figure 7(a) shows that as the SiO_2 content increases from 5% to 25%, the shrinkage in the *X* direction increases from 1.69% to 2.06%, then decreases to 1.94%, in the *Y* direction increases from 3.04% to 3.39%, then decreases to 3.24%, and in the *Z* direction increases from 1.38% to 2.25%, decreases to 1.87%, then increases to 2.53%. It is worth noting that in both the *X* and *Y* directions, the shrinkage trend decreases before increasing, while in the *Z* direction, it increases first, then decreases, and finally increases again. This behavior is attributed to the evolution of the mullite phase during the solid-state reaction. As the SiO_2 content increases, more mullite is formed; since the formation of mullite is accompanied by volume expansion, the initial volume expansion exceeds the shrinkage caused by pore elimination

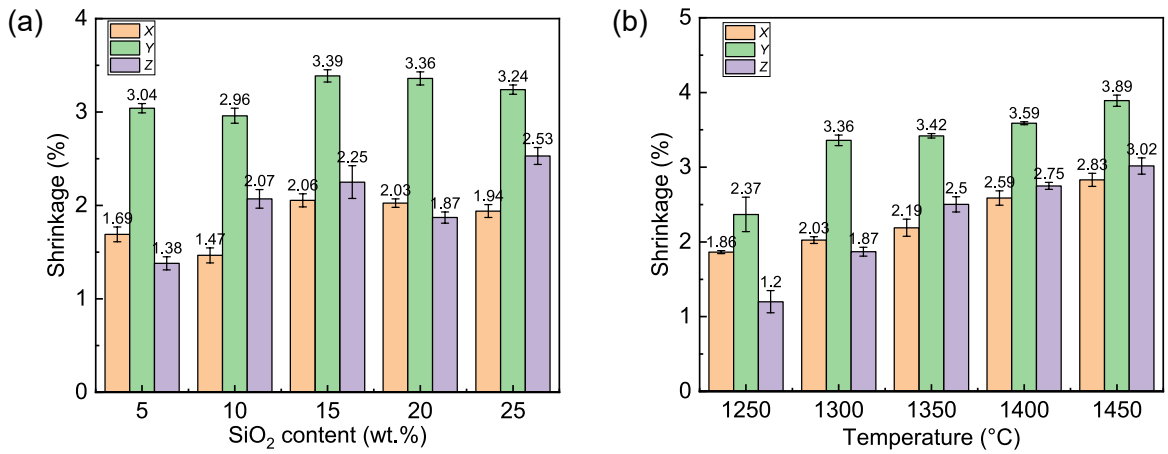


Fig. 7: Shrinkage of ceramic cores with different SiO_2 contents sintered at 1,300 °C (a) and with 20% SiO_2 sintered at different temperatures (b)

and liquid phase sintering, therefore, the overall shrinkage decreases. However, as SiO_2 further increases, the additional liquid phase promotes sintering to a greater extent, causing the shrinkage to increase again. The shrinkage trend in the *Z* direction is primarily attributed to the presence of interlayer gaps. As UV-curing printing proceeds layer by layer, the ceramic powder is deposited under the action of gravity. This leads to an uneven distribution where each layer is characterized by a resin-rich top and a powder-rich bottom, thereby resulting in the formation of interlayer gaps[38]. During the ceramic sintering process, the interlayer gaps shrink rapidly[39, 40]. At low SiO_2 levels, the volume expansion caused by mullite formation is relatively small compared to the shrinkage caused by interlayer gap closure and overall sintering densification, therefore, the shrinkage gradually increases. When the SiO_2 content reaches about 20%, the expansion effect of mullite dominates the gap shrinkage and densification, resulting in a decrease in shrinkage. As SiO_2 continues to increase above 20%, the liquid phase generated during sintering becomes more prevalent, which improves the degree of densification and increases shrinkage. This behavior reflects the complex interaction between phase transformation-induced expansion and densification processes during sintering.

As shown in Fig. 7(b), the shrinkage rate in the *X* direction increases from 1.86% to 2.83%, in the *Y* direction from 2.37% to 3.89%, and in the *Z* direction from 1.20% to 3.02% as the sintering temperature increases from 1,250 °C to 1,450 °C. The sintering temperature is positively correlated with the shrinkage rate, which is consistent with the fact that the increase in temperature enhances the degree of sintering densification. The increase in sintering temperature also increases the sintering driving force of the ceramic core, promotes densification, and increases the sintering neck[41]. Due to the existence of interlayer gaps, the increase rate of shrinkage in the *Z* direction is fast at first and then slows down. When the sintering temperature is low, the effect of the interlayer gap is large, and the shrinkage degree in the *Z* direction changes greatly. However, when the sintering temperature is high, the degree of densification is high, so the effect of the interlayer gap is small, and the shrinkage degree in the *Z* direction does not change much.

The reason for the greater shrinkage in the *Y* direction compared to the *X* direction is illustrated in Fig. 8. The laser scanning direction aligns with the scraper movement direction, unidirectional scanning along the *X*-direction causes the energy distribution to concentrate in *Y*-direction. This leads to an accumulation of curing shrinkage, resulting in more obvious shrinkage along the *Y*-direction after sintering.

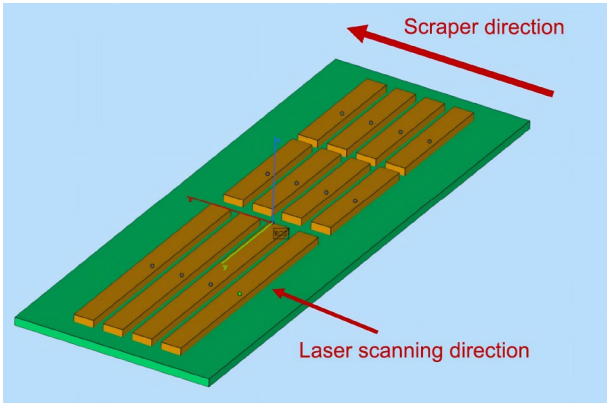


Fig. 8: Samples and SLA printing direction

3.3 Influence of SiO_2 content and sintering temperature on open porosity and bulk density

Figure 9(a) shows the change curves of the open porosity and bulk density of the ceramic core with the increase of SiO_2 content (sintered at 1,300 °C). It can be seen that with the increase of SiO_2 content from 5% to 25%, the open porosity decreases from 23.2% to 20.8%, and the bulk density decreases from 1.44 g·cm^{-3} to 1.36 g·cm^{-3}. With the increase of SiO_2 content, these fine powder particles fill the pores of large particles, as shown in Fig. 2(c), which reduces the open porosity. The ceramic powder contains impurities such as Fe, which form the liquid phase with SiO_2, therefore, as the SiO_2 content increases, the liquid phase content also increases, promotes sintering densification, and reduces the porosity. Although sintering densification reduces the volume of ceramic core and increases its bulk density, the overall bulk density of the ceramic core decreases with the increase of SiO_2 content. This is because the intrinsic density of SiO_2 is lower than that of Al_2O_3.

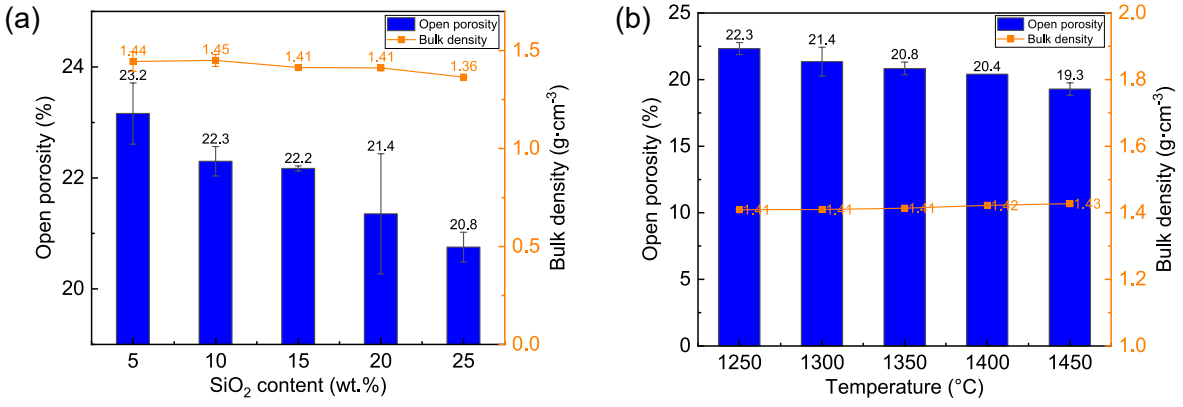


Fig. 9: Open porosity and bulk density of ceramic cores with different SiO_2 contents sintered at 1,300 °C (a) and with 20% SiO_2 sintered at different temperatures (b)

Figure 9(b) shows the change curves of the open porosity and bulk density with sintering temperature (with 20% SiO_2). With the increase of sintering temperature from 1,250 °C to 1,450 °C, the open porosity decreases from 22.33% to 19.3%, while the bulk density increases from 1.41 g·cm^{-3} to 1.43 g·cm^{-3}. This is consistent with the sintering theory that the open porosity decreases with the increase of sintering temperature[28, 42]. With the increase of sintering temperature, the driving force of sintering densification increases[43], and the densification process leads to the elimination of pores and suppresses further grain growth[44, 45]. The sintering temperature is negatively correlated with the open porosity of the ceramic core and positively correlated with the bulk density. Therefore, it serves as a critical parameter governing these physical properties. The increase of SiO_2 content and sintering temperature reduces the open porosity of ceramic cores, but their effects on bulk density are opposite. Generally, while the driving force of densification increases with the increase of sintering temperature, this factor has a less effect on bulk density compared to the addition of low-density SiO_2. Notably, the porosity of ceramic cores obtained at 1,450 °C is only 19.3%, and such a low level of porosity will severely impede the removal of cores.

3.4 Influence of SiO_2 content and sintering temperature on flexural strength and deflection

Figure 10(a) shows the room temperature flexural strength variation curve of the ceramic cores with SiO_2 content ranging from 5% to 25% (sintered at 1,300 °C). The ceramic core with 5% SiO_2 exhibits the lowest flexural strength of 8.34 MPa, while the ceramic core contained 20% SiO_2 shows the highest flexural strength of 15.06 MPa. When the SiO_2 content is low, increasing SiO_2 helps to improve the flexural strength, and the SiO_2 at high temperatures can react with Al_2O_3 to form mullite, which prevents the expansion of microcracks within the core, thus improving the flexural strength. When the SiO_2 content reaches 20%, the flexural strength reaches a peak. However, excessive SiO_2 reduces the flexural strength. When the content of SiO_2 is too high, the amount of liquid phase formed by residual SiO_2 and impurities such as Fe also increases, distributed between the alumina particles, weakening the bonding force between the alumina particles, so that the microcracks in the ceramic core are easy to expand along the boundaries of the alumina particles under the action of external forces, reducing the strength of the core.

Figure 10(b) shows the variation of flexural strength with sintering temperature (with 20% SiO_2). The ceramic core obtained at 1,250 °C has the lowest flexural strength of 13.26 MPa. The ceramic core obtained at 1,450 °C has the highest flexural strength of 36.33 MPa. The flexural strength is positively correlated with the sintering temperature. The driving force of densification increases with the increase of sintering temperature[43], so that the ceramic core is more compact. At the same time, the 1 μm SiO_2 particles fill the gaps between the larger Al_2O_3 particles, inhibiting the growth of the particles, thereby improving the flexural strength.

Figure 11(a) shows the change in flexural strength of the core contained 20% SiO_2 with sintering temperature measured at 1,350 °C. The flexural strength increases with the increase of sintering temperature. It is the lowest at 1,250 °C (16.36 MPa) and the highest at 1,450 °C (28.05 MPa). When the sintering temperature is lower than the test temperature (1,350 °C), the ceramic core is re-sintered during the heat preservation, and the flexural strength increases. When the sintering temperature exceeds 1,350 °C, the previously unsintered parts will continue to sinter, causing the ceramic to become denser and increasing the flexural strength of the ceramic cores. As shown in Fig. 3(e), numerous sintered necks form between SiO_2 particles, with fine Al_2O_3 particles distributed among large Al_2O_3 particles. This interconnected microstructure contributes to the exceptionally high flexural strength of the ceramic core[41]. According to the XRD and EDS results, the sintered necks are mainly composed of SiO_2 and mullite. Mullite is formed by the solid phase reaction between SiO_2 and Al_2O_3, which significantly enhances the high-temperature flexural strength of ceramic cores[46].

Figure 11(b) shows the change of high-temperature deflection measured at 1,350 °C. The high-temperature deflection of ceramic cores decreases as the sintering

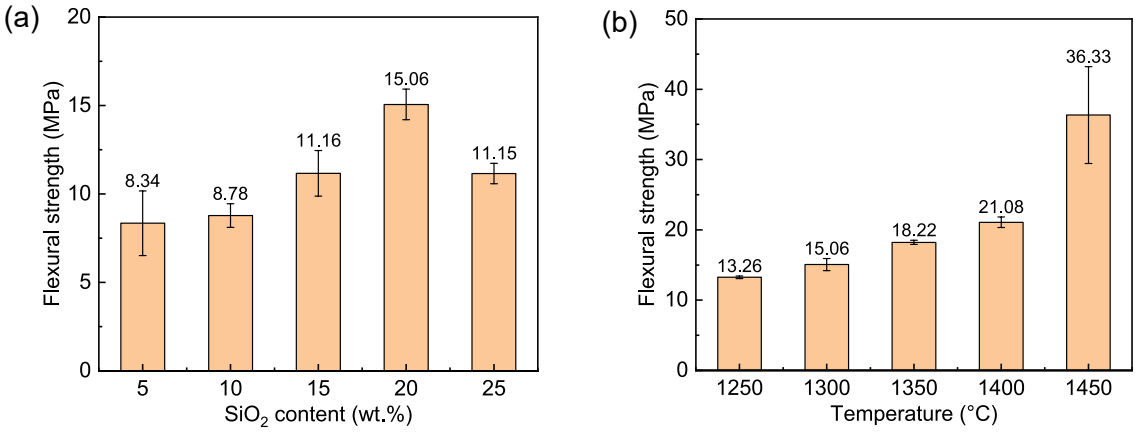


Fig. 10: Flexural strength of Al_2O_3 ceramic cores after sintering: (a) with different SiO_2 contents sintered at 1,300 °C; (b) with 20% SiO_2 sintered at different sintering temperatures

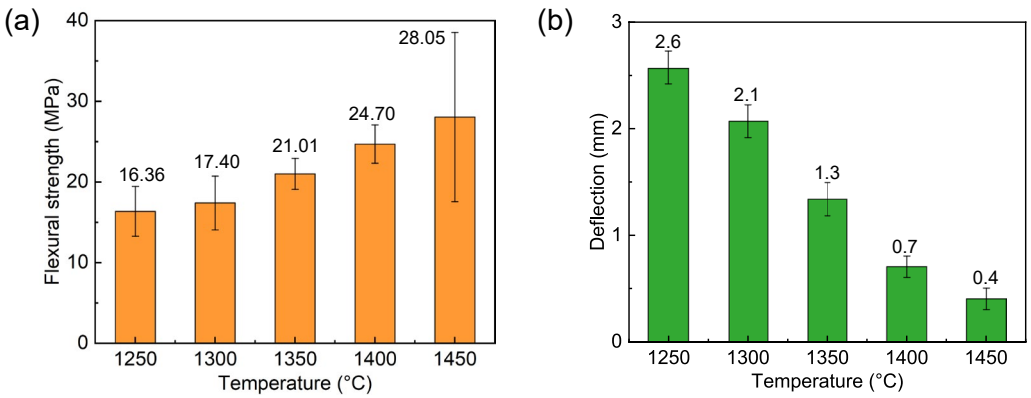


Fig. 11: High temperature properties of Al_2O_3 ceramic cores (with 20% SiO_2) after sintering measured at 1,350 °C: (a) flexural strength; (b) deflection

temperature increases. Specifically, the maximum deformation of 2.6 mm is observed at a sintering temperature of 1,250 °C, whereas the minimum deformation of 0.4 mm is recorded at 1,450 °C. With the increase of sintering temperature, a greater proportion of SiO_2 and Al_2O_3 participates in the solid phase reaction, leading to an increase in mullite content. Given the excellent high-temperature properties of mullite, this phase evolution significantly reduces the high-temperature deflection.

As shown in Fig. 12(a), after debinding, the degree of densification is low, and the particles are relatively loose. As the temperature increases to 1,250 °C, as shown in Fig. 12(b), the SiO_2 particles generate sintering necks, the sintering degree is improved, and the strength is improved. When the temperature continues to rise to 1,300 °C, as shown in Fig. 12(c), the sintering necks are generated between the small Al_2O_3 particles and the SiO_2 particles, the solid phase reaction occurs and mullite is generated, therefore, the degree of densification is improved, and the flexural strength is also improved. When the temperature reaches 1,450 °C, as shown in Fig. 12(d), the sintering necks are formed between the large particles and the small particles, the degree of densification is high, and the flexural ceramic strength is greatly improved.

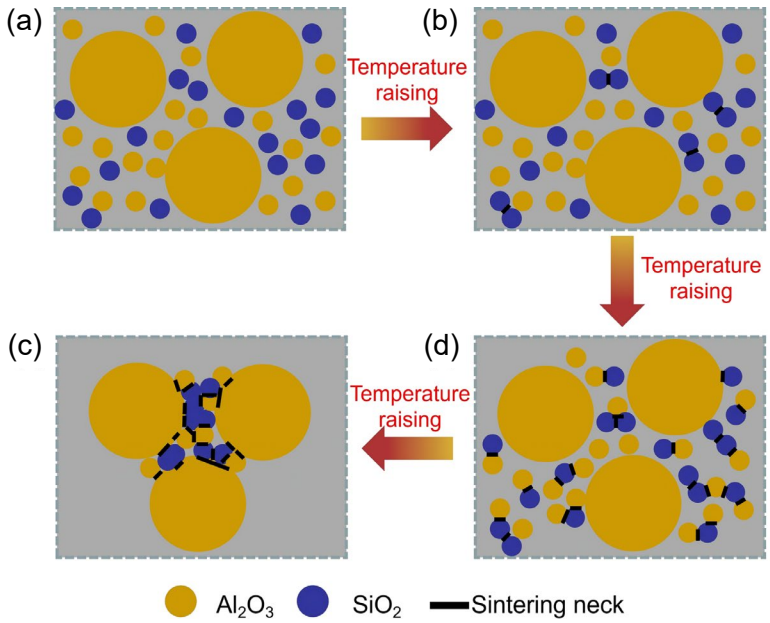


Fig. 12: Diagram of sintering mechanism: (a) after debinding; (b) 1,250 °C; (C) 1,300 °C; (d) 1,450 °C

4 Conclusions

Al_2O_3 ceramic slurry with high solid contents was prepared, and Al_2O_3 ceramic core specimens were successfully prepared using SLA technology. The effects of SiO_2 content and sintering temperature on performance of Al_2O_3 ceramic cores were studied:

(1) In Al_2O_3 ceramic cores, large particles serve as a structural framework, while small particles fill the interstitial gaps. The small particles initially form sintering necks. As the SiO_2 content increases, the intensity of the SiO_2 phase peak first increases and then decreases; this is because the formation of the mullite phase consumes a certain amount of SiO_2. As the temperature rises, sintering necks also form on the surfaces of the large particles, leading to the corresponding increase in flexural strength. When the sintering temperature exceeds 1,350 °C, the intensity of the mullite phase peak gradually increases with rising temperature.

(2) At 1,300 °C, when the SiO_2 content reaches 25%, more mullite is formed, small particles adhere to the surface of large

particles and form sintering necks. The shrinkage of ceramic cores first increases and then decreases as the SiO_2 content rises. This is determined by a combination of the volume expansion resulting from the densification of the ceramic during sintering and the formation of mullite, as well as the interlayer voids. As the sintering temperature increases, the shrinkage of the ceramic cores continues to rise.

(3) The increase in SiO_2 content and sintering temperature reduces the open porosity, but have the opposite effect on the packing density. When the SiO_2 content is low, increasing SiO_2 helps to improve the flexural strength, but excessive SiO_2 reduces the flexural strength. The sintering temperature is positively correlated with the flexural strength and negatively correlated with the high-temperature deflection. When the SiO_2 content is 20% and the sintering temperature is 1,400 °C, the performance of the ceramic core is the best, with an open porosity of 20.4%, a bending strength of 21.07 MPa, and a deflection of 0.7 mm.

Acknowledgment

This work was financially supported by the Joint Foundation Project of Liaoning (Grant No. 2024-MSLH-509), China.

Conflict of interest

The authors declare that they have no conflicts of interest.

References

[1] Yang F Q. Research on high quality cone beam CT imaging technology of turbine blade based on knowledge. Doctoral Dissertation, Xi'an: Northwestern Polytechnical University, 2018: 12–13. (In Chinese)
[2] Tong W T. Analysis of precision forming technology for aircraft engine turbine blades. Internal Combustion Engine & Accessories, 2020(19): 36–37. (In Chinese)
[3] Chen X. Research on high temperature performance of alumina ceramic core for turbine blades. Master's Dissertation, Harbin: Harbin Institute of Technology, 2011: 8–9. (In Chinese)
[4] Li D C, Lu Z L, Tian X Y, et al. Additive manufacturing – A transformational technology for aerospace manufacturing. Chinese Journal of Aeronautics, 2022, 43(4): 22–38, 41. (In Chinese)
[5] Ma Y T, Yin S K, Yu R L, et al. Research progress of light-curing 3D printing ceramic core technology. Foundry, 2022, 71(3): 271–276. (In Chinese)
[6] Meng X T. Research on the microstructure and properties of alumina ceramic materials manufactured by photopolymerization additive method. Master's Dissertation, Shenyang: Northeast University, 2021: 11–12. (In Chinese)
[7] Ma Y T. Basic research on the preparation process of 3D printed silicon-based ceramic cores. Master's Dissertation, Beijing: China Academy of Machinery Science & Technology, 2023: 10–11. (In Chinese)
[8] Jia H Y. Research on the microstructure and properties of UV cured 3D printed ceramic cores. Master's Dissertation, Shenyang: Shenyang University of Technology, 2019: 11–12. (In Chinese)
[9] Liang Q R, Wu Y S, Liu X F, et al. Research progress on ceramic cores for casting turbine blades of aircraft engines. Foundry, 2018, 67(9): 790–793. (In Chinese)
[10] Wereszczak A A, Breder K, Ferber M K, et al. Dimensional changes and creep of silica core ceramics used in investment casting of superalloys. Journal of Materials Science, 2002, 37(19): 4235–4245.
[11] Xu S F and Wu J Q. Preparation method of ceramic core. Foshan Ceramics, 2019, 29(2): 3–8. (In Chinese)
[12] Liu X Y, Wang B S, and Zhang L T. Research progress on alumina based ceramic cores. Aviation Manufacturing Technology, 2005(7): 26–29. (In Chinese)
[13] Cao L M. Process characteristics of foreign oriented and single crystal hollow blade cores. Materials Engineering, 1995(5): 20–21, 31. (In Chinese)
[14] Liang C, Liu W, Liu Q, et al. The formation of core-sheath structure and its effects on thermal decomposition and crystallization of alumina fibers. Ceramics International, 2020: 47(4): 5145–5155.
[15] Li Z Y, Song Y F, Yang Z G, et al. Research on properties of alumina ceramic core for gel casting hollow blade. Foundry, 2020, 69(5): 475–479. (In Chinese)
[16] Wang S C, Zhu Y W, Wu Y, et al. Development and application of photopolymerization 3D printing technology and photosensitive resin. Journal of Functional Polymer, 2022, 35(1): 19–35.
[17] Bae C J and Halloran J W. Influence of residual monomer on cracking in ceramics fabricated by stereolithography. International Journal of Applied Ceramic Technology, 2011, 8(6): 1289–1295.
[18] Li X, Gao M, and Jiang Y. Microstructure and mechanical properties of porous alumina ceramic prepared by a combination of 3D printing and sintering. Caremics International, 2016: 12531–12535.
[19] Nakajima A and Messing G L. Liquid-phase sintering of alumina coated with magnesium aluminosilicate glass. Journal of the American Ceramic Society, 2010, 81(5): 1163–1172.
[20] Zhang K, He R, Ding G, et al. Effects of fine grains and sintering additives on stereolithography additive manufactured Al_2O_3 ceramic. Ceramics International, 2021, 47(2): 2303–2310.
[21] Wu H, Cheng Y, Liu W, et al. Effect of the particle size and the debinding process on the density of alumina ceramics fabricated by 3D printing based on stereolithography. Ceramics International, 2016, 42(15): 17290–17294.
[22] Zhou M, Liu W, Wu H, et al. Preparation of a defect-free alumina cutting tool via additive manufacturing based on stereolithography – Optimization of the drying and debinding processes. Ceramics International, 2016, 42(10): 11598–11602.
[23] Li H, Liu Y, Liu Y, et al. Effect of burying sintering on the properties of ceramic cores via 3D printing. Journal of Manufacturing Processes, 2020, 57: 380–388.
[24] Xing Z W, Liu W W, Chen Y, et al. Effect of plasticizer on the fabrication and properties of alumina ceramic by stereolithography-based additive manufacturing. Ceramics International, 2018, 44(16): 19939–19944.
[25] Li H, Liu Y, Liu Y, et al. Evolution of the microstructure and mechanical properties of stereolithography formed alumina cores sintered in vacuum. Journal of the European Ceramic Society, 2020, 40(14): 4825–4836.
[26] Tang S, Yang L, Liu X, et al. Direct ink writing additive manufacturing of porous alumina-based ceramic cores modified with nanosized MgO. Journal of the European Ceramic Society, 2020, 40(15): 5758–5766.
[27] Li H, Liu Y, Liu Y, et al. Effect of sintering temperature in argon atmosphere on microstructure and properties of 3D printed alumina ceramic cores. Journal of Advanced Ceramics, 2020, 9(2): 220–231.

[28] Li Q, An X, Liang J, et al. Balancing flexural strength and porosity in DLP-3D printing Al_2O_3 cores for hollow turbine blades. Journal of Materials Science & Technology, 2022, 104: 19–32.
[29] Li X, Su H, Dong D, et al. Enhanced comprehensive properties of stereolithography 3D printed alumina ceramic cores with high porosities by a powder gradation design. Journal of Materials Science & Technology, 2022, 131(36): 264–275.
[30] Yang Z G, Yu J B, Deng K, et al. The influence of silicone resin on the preparation and strengthening effect of porous alumina based ceramics. Journal of Artificial Crystals, 2015, 44(12): 3515–3520.
[31] Jiang W, Li K, Xiao J, et al. Effect of silica fiber on the mechanical and chemical behavior of alumina-based ceramic core material. Journal of Asian Ceramic Societies, 2017, 5(4): 410–417.
[32] Qin Y and Pan W. Effect of silica sol on the properties of alumina-based ceramic core composites. Materials Science & Engineering, 2009, 508(1–2): 71–75.
[33] Li H, Liu Y, Liu Y, et al. Silica strengthened alumina ceramic cores prepared by 3D printing. Journal of the European Ceramic Society, 2021, 41(4): 2938–2947.
[34] Wang X, Zhou Y, Zhou L, et al. Microstructure and properties evolution of silicon-based ceramic cores fabricated by 3D printing with stair-stepping effect control. Journal of the European Ceramic Society, 2021, 41(8): 4650–4657.
[35] Wang R F, Liu Z Y, Lin M, et al. The influence of different mineralizers on the properties of aluminum based ceramic cores. Stanford Materials, 2012, 26(20): 115–118.
[36] Hughes S W. Archimedes revisited: A faster, better, cheaper method of accurately measuring the volume of small objects. Physics Education, 2005, 40(5): 468–474.
[37] Chen I W and Wang X H. Sintering dense nanocrystalline ceramics without final-stage grain growth. Nature, 2000, 404(6774): 168–171.
[38] Chen D D, Bao M D, Li X, et al. Research on the anisotropy of 3D printed silicon-based ceramic cores. China Caremics, 2020, 56(5): 33–39. (In Chinese)
[39] Li Q L, Chen T C, Liang J J, et al. Manufacturing of ceramic cores: From hot injection to 3D printing. Journal of Materials Science & Technology, 2023, 134: 95–105.
[40] Li Q L, Hou W Q, Liang J J, et al. Controlling the anisotropy behaviour of 3D printed ceramic cores: From intralayer particle distribution to interlayer pore evolution. Additive Manufacturing, 2022, 58: 103055.
[41] Yang Z G, Zhao Z J, Yu J B, et al. Effect of silicone resin as precursor and binder on the properties of alumina-based ceramic cores using ball-shaped powders. Ceramics International, 2019, 45: 2170–2177.
[42] Ma J and Lim L C. Effect of particle size distribution on sintering of agglomerate-free submicron alumina powder compacts. Journal of the European Ceramic Society, 2002, 22(13): 2197–2208.
[43] Li H, Liu Y, Li W, et al. The effect of sintering on the properties of calcium oxide promoted alumina-based ceramic cores via 3D printing. Materials Chemistry and Physics, 2021, 263: 12443.
[44] Guo S Q. Densification of ZrB_2-based composites and their mechanical and physical properties: A review. Journal of the European Ceramic Society, 2009, 29(6): 995–1011.
[45] Funahashi S, Guo J, Guo H Z, et al. Demonstration of the cold sintering process study for the densification and grain growth of ZnO ceramics. Journal of the American Ceramic Society, 2017, 100(2): 546–553.
[46] Li Q L, Meng X T, Zhang X C, et al. Enhanced 3D printed Al_2O_3 core via in-situ mullite. Additive Manufacturing, 2022, 55: 102826.